MoS_2/Graphene Composite Anodes with Enhanced Performance for Sodium-Ion Batteries: The Role of the Two-Dimensional Heterointerface

*Xiuqiang Xie, Zhimin Ao, Dawei Su, Jinqiang Zhang, and Guoxiu Wang**

Graphene has been widely used as conformal nanobuilding blocks to improve the electrochemical performance of layered metal sulfides (MoS_2, WS_2, SnS, and SnS_2) as anode materials for sodium-ion batteries. However, it still lacks in-depth understanding of the synergistic effect between these layered sulfides and graphene, which contributes to the enhanced electroactivity for sodium-ion batteries. Here, MoS_2/reduced graphene oxide (RGO) nanocomposites with intimate two-dimensional heterointerfaces are prepared by a facile one-pot hydrothermal method. The heterointerfacial area can be effectively tuned by changing the ratio of MoS_2 to RGO. When used as anode materials for sodium-ion batteries, the synergistic effect contributing to the enhanced reversible capacity of MoS_2/RGO nanocomposites is closely related with the heterointerfacial area. The computational results demonstrate that Na prefers to be adsorbed on MoS_2 in the MoS_2/RGO heterostructure rather than intercalate into the MoS_2/RGO heterointerface. Interestingly, the MoS_2/RGO heterointerfaces can significantly increase the electronic conductivity of MoS_2, store more Na ions, while maintaining the high diffusion mobility of Na atoms on MoS_2 surface and high electron transfer efficiency from Na to MoS_2. It is expected that the efforts to establish the correlation between the two-dimensional heterointerface and the electrochemical sodium-ion storage performance offer fundamental understanding for the rational design of layered metal sulfides/graphene composites as high-performance electrode materials for sodium-ion batteries.

1. Introduction

As one of the promising state-of-the-art battery systems, sodium-ion batteries (SIBs) have attracted tremendous attention as an alternative to lithium-ion batteries (LIBs). The interest in SIBs stems from the advantages of the Na element for battery applications, including its abundance in nature, low cost, and negative redox potential (–2.71 V vs SHE).[1] However, the practical applications of SIBs have been hamstrung by the lack of suitable anode materials to host Na^+, which has a larger radius than that of Li^+. Graphite with a highly ordered structure is considered to be not suitable to accommodate Na^+ because Na hardly forms staged intercalation compounds with graphite.[2] Two-dimensional layered metal sulfides (LMSs) with analogous structures to graphite, such as MoS_2,[3] WS_2,[4] SnS,[5] and SnS_2,[6] have been reported as potential electrode materials for SIBs. The open framework of these types of materials allows Na^+ to insert reversibly with acceptable mobilities. However, the further application of 2D LMSs is impeded by their inherent limitations. First, these semiconductor metal sulfides have inherently low electronic conductivity, which affects their electrochemical performances for Na^+ storage. Second, owing to the high surface energy and interlayer van der Waals attractions,[7] these thermally unstable 2D nanomaterials have a tendency to restack to minimize the surface energy. Furthermore, the significant volume change and mechanical stress as a concomitant of sodium-ion insertion and extraction can induce the failure of the electrode and the loss of contact between active materials and the current collector, resulting in poor cycling stability.

Graphene has established itself as a promising candidate to circumvent these challenges. For example, WS_2/graphene,[4] SnS/graphene,[5b] and SnS_2/graphene[6] nanocomposites have already been successfully applied as anode materials for SIBs, showing a synergistic effect for sodium-ion storage, including improved capacity, rate capability, and cycling stability. In these reports, it is generally recognized that the enhanced electrochemical performances are attributed to the good electronic conductivity and mechanical resilience of graphene as 2D conformal building blocks for these layered sulfides. However, a fundamental understanding of the exact interaction mechanism between LMSs and graphene for improving Na^+ storage performance is still not clear. The heterointerface between LMSs and graphene has been proven to contribute to novel properties and new functionalities that cannot be achieved by individual constituting materials.[8] Therefore, investigations

X. Xie, Dr. Z. Ao, Dr. D. Su, J. Zhang, Prof. G. Wang
Centre for Clean Energy Technology
School of Chemistry and Forensic Science
University of Technology Sydney
Broadway, Sydney, NSW 2007, Australia
E-mail: guoxiu.wang@uts.edu.au
Prof. G. Wang
College of Material Science & Engineering
Nanjing University of Aeronautics and Astronautics
Nanjing, P.R. China

DOI: 10.1002/adfm.201404078

on the role of the heterointerface for sodium ion storage in LMSs/graphene composites could enhance the in-depth understanding of the synergistic effect between LMSs and graphene. Compared to other LMSs/graphene composites such as particles/graphene nanocomposites[9] and nanotubes/graphene nanocomposites,[10] 2D materials with LMS nanosheets on the surface of graphene nanosheets have attracted considerable attentions.[11] Since this sheet-on-sheet structure can provide large interfacial areas, it is important to investigate the role of heterointerfaces for sodium-ion storage in LMSs/graphene composites.

In this work, by taking MoS_2 as a typical example, we established the correlations between the 2D heterointerface and the sodium-ion storage performance of LMSs/graphene composites. MoS_2/reduced graphene oxide (RGO) nanocomposites were prepared by a facile hydrothermal method using phosphomolybdic acid, L-cysteine, and GO as precursors. The sheet-on-sheet MoS_2/RGO nanocomposites were formed, which effectively suppresses agglomeration of MoS_2 and RGO. Furthermore, MoS_2/RGO nanocomposites with different MoS_2/RGO heterointerfacial areas were prepared by changing the ratio of MoS_2 to RGO and applied as anode materials to investigate the role of the 2D MoS_2/RGO heterointerface for Na^+ storage. It is found that the synergistic effect contributing to the enhanced reversible capacity of MoS_2/RGO nanocomposites is closely related to the heterointerfacial area. First-principles calculations were performed to investigate Na atoms adsorption and diffusion on MoS_2 and the MoS_2/RGO heterointerface, respectively. The corresponding band structure of MoS_2 and the MoS_2/RGO heterointerface and electron transfer between Na atoms and MoS_2 or the MoS_2/RGO heterointerface were also considered. The computational results demonstrate that Na prefers to be adsorbed on MoS_2 in the MoS_2/RGO heterostructure (Na/MoS_2/RGO) rather than intercalate into the MoS_2/RGO heterointerface (MoS_2/Na/RGO). Moreover, the 2D MoS_2/RGO heterointerface can significantly increase the conductivity of MoS_2, capture more Na atoms, while maintaining high diffusion mobility of Na atoms on the MoS_2 surface and high electron transfer efficiency from Na to MoS_2. This work could not only enrich the functionalities of the MoS_2/RGO heterostructure, but also clarify the synergistic effect between MoS_2 and RGO for the enhancement of electrochemical Na-ion storage in MoS_2/RGO composites. The outcomes could facilitate the rational design of other 2D TMSs/graphene nanoassemblies as high performance electrode materials for Na-ion batteries.

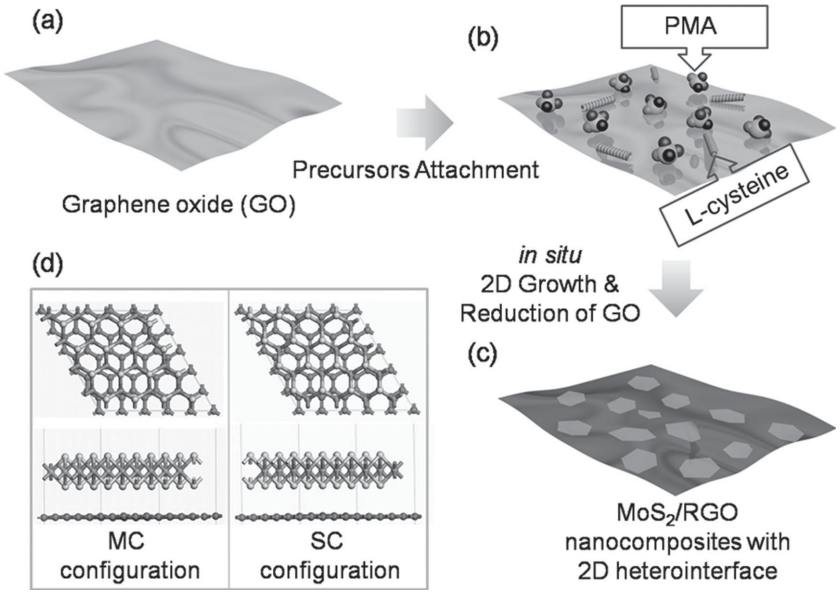

Figure 1. Schematic illustration for the preparation of MoS_2/RGO heterostructures. As shown in (d), there are two possible stacking configurations: MC (Mo on top of C atoms) and SC (S on top of C atoms) configurations. The yellow, green, and gray atoms represent S, Mo, and C atoms, respectively.

2. Results and Discussions

MoS_2/RGO nanocomposites have been synthesized as anode materials for Na-ion batteries by incorporating RGO with presynthesized MoS_2.[12] However, in order to realize the functionalities of the 2D MoS_2/RGO heterointerface, it is required to prepare high-quality electrical contact between MoS_2 and RGO. Sheet-on-sheet structured MoS_2/RGO composites with controllable heterointerfaces were synthesized by a hydrothermal method, followed by a calcination process (as shown in **Figure 1**). GO is highly dispersible in water due to the existence of hydrophilic groups (hydroxyl, carboxyl, and epoxy groups), which makes it a favorable precursor for the aqueous synthesis of RGO-based nanoarchitectures. Phosphomolybdic acid ($H_3PMo_{12}O_{40}\cdot xH_2O$, PMA) is used as molybdenum precursor. In the first step, GO aqueous suspension was mixed with PMA and L-cysteine by mechanical stirring at room temperature. The PMA molecule is abundant in oxygen-containing functional groups and double bonds (see the molecular structure model of PMA in Figure S1, Supporting Information), which can be attracted to graphene oxide through the noncovalent hydrogen bonds and the π–π interaction between the double bond in PMA and the conjugated RGO basal planes (Figure 1b). The PMA/L-cysteine/GO mixture was then transferred to an autoclave and subjected to hydrothermal treatment at 200 °C for 24 h. The oxygenated functional groups on the GO surface can act as nucleation sites for MoS_2, leading to the formation of MoS_2 crystal nucleus on the RGO surface.[13] Under hydrothermal conditions, PMA is transformed in situ to the MoS_2 nucleus in the presence of L-cysteine. Simultaneously, GO is reduced to RGO by H_2S released from L-cysteine. L-cysteine could form a polymeric network structure under the solution-phase reaction, which facilitated the formation of MoS_2 with a two-dimensional structure.[14] The following crystal growth leads to the formation of 2D MoS_2 nanosheets covering the RGO basal plane, creating MoS_2/RGO heterointerfaces (Figure 1c). MoS_2/RGO composites were then subjected to high temperature calcination at 800 °C under Ar atmosphere, which further enhances the

interfacial interaction between MoS_2 and RGO by increasing the crystallinity of MoS_2 (Figure S2, Supporting Information) and reducing the residual oxygen moieties (Table S1, Supporting Information). By increasing the stock of PMA, the weight ratio of MoS_2 and RGO can be tuned. In this way, three MoS_2/RGO composites with different MoS_2 to RGO ratios were prepared (denoted as MG-*x*, $x = 1, 2, 3$). As shown in Figure 1d, there are two possible MoS_2/RGO heterostructures: MC (Mo on the top of C atoms) and SC (S on the top of C atoms) structures. The total energy of the MC structure is only 11.8 meV C^{-1}, which is lower than that of SC, suggesting that both of the two structures are possible. The distances between MoS_2 and RGO layers in MC and SC bilayers are 3.35 and 3.36 Å, respectively. The interaction energy between MoS_2 and RGO layers (E_{int}) is calculated to be –0.02 and –0.01 eV C^{-1} for MC and SC bilayers, respectively, indicating the weak van der Waals interaction between MoS_2 and RGO (see the theoretical calculations in the Supporting Information).

Through thermogravimetric analysis (TGA), the MoS_2 weight ratios in MG-*x* composites were determined to be 44.2% (MG-1), 49% (MG-2), and 68.7% (MG-3), respectively (as shown in Figure S3, Supporting Information). **Figure 2** shows the X-ray diffraction (XRD) patterns of bare RGO, MoS_2, and the as-prepared MG-*x* samples. For bare RGO, a broad peak at 25.4° is discernable, which is the characteristic peak due to the random restacking of RGO layers during hydrothermal synthesis. However, for MoS_2/RGO composites, the intensity of the RGO diffraction peak decreased and disappeared with the increase of the MoS_2 ratio, suggesting that the percentage of MoS_2 in the MG-*x* samples is crucial for preventing the aggregation of RGO layers. It is clearly indicated that 2H–MoS_2 phases have formed in all of these samples as evidenced by peaks at 14.4°, 32.8°, 39.5°, 49.8°, 58.3°, and 60.1°. The diffraction peaks correspond to the (002), (100), (103), (105), (110), and (008) planes of 2H–MoS_2 (JCPDS Card No. 37–1492). 2H–MoS_2 is structural analog of graphene, the basal (002) crystal planes of which are held together by van der Waals forces along *c*-axis. It should be noted that the intensity ratio of (002) and (100) peak of MoS_2 nanosheets ($I_{(002)}/I_{(100)}$) varies according to MoS_2 ratio, which decreases in the order MG-1 (2.67) > MG-2 (2.16) > MG-3 (1.30). Therefore, the (002) plane growth of MoS_2 crystals is restrained due to the incorporation

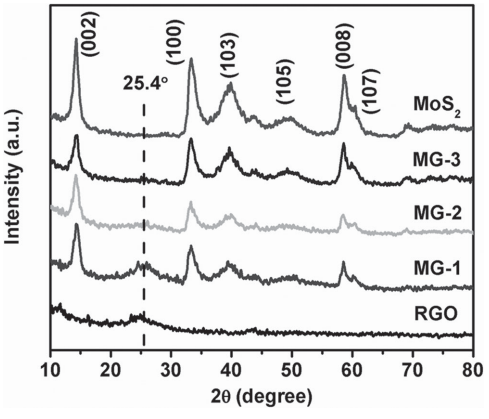

Figure 2. XRD patterns of RGO, MG-1, MG-2, MG-3, and MoS_2.

of RGO in MG-*x* nanocomposites. The disappearance of the RGO (002) peak and the decrease of the MoS_2 (002) peak indicate the evolution of the MoS_2/RGO heterointerface with the increase of the MoS_2 ratio. Raman characterization confirms that the as-prepared product is composed of RGO and MoS_2 (Figure S4, Supporting Information). Using energy-dispersive X-ray (EDX) spectroscopy, the O/C atomic ratios in MG-1, MG-2, and MG-3 were determined to be 0.15, 0.10, and 0.07, respectively (Table S2, Supporting Information).

The microstructures of MG-*x* heterostructures were analyzed by scanning electron microscopy (SEM) and transmission electron microscopy (TEM). **Figure 3** shows the SEM images of MG-*x*, providing a general view of the morphology over a large scale. Bare MoS_2 obtained from the same experimental procedure without RGO tends to aggregate due to the high surface energy and interlayer van der Waals attraction,[7a,15] leading to the formation of three-dimensional flower-like agglomerations assembled by MoS_2 nanosheets (Figure S5, Supporting Information). With the presence of RGO in the mixture, the MG-*x* composites show a curved thin flaky morphology as shown in Figure 3, which is composed of MoS_2 nanosheets grown parallel to RGO. The morphology is different from the previously reported MoS_2/RGO nanoarchitectures prepared from either Na_2MoO_4 or $(NH_4)_2MoS_4$ as Mo-source, where MoS_2 nanoparticles formed.[9,13,16] No MoS_2 agglomerations were formed in the MG-*x* composites, which suggests that RGO can stabilize MoS_2 nanosheets. The formation of separated MoS_2 nanosheets is favorable for the accessibility of reaction sites for Na^+. Moreover, as shown in Figure 3b,c,f, MoS_2 ingredient has an intimate contact with RGO and no isolated MoS_2 was observed in all the three MG-*x* nanocomposites. With the increase of the ratio of MoS_2, the coverage of MoS_2 nanosheets on the RGO matrix increases correspondingly, which is in agreement with the XRD results. The elemental mapping images shown in Figure S6 (Supporting Information) clearly illustrate that MoS_2 nanosheets are completely encapsulated within RGO.

The high-resolution TEM (HRTEM) images of the curled edge shown in **Figure 4**b,d,f reveal lattice fringes with an interplanar spacing of 0.62 nm, which can be indexed as the (002) lattice planes of 2H–MoS_2. The van der Waals interfacial interaction between RGO and MoS_2 is strong enough to firmly bind MoS_2 with RGO. Even after long-term ultrasonic dispersion for TEM characterization, MoS_2 nanosheets are anchored onto the RGO substrate and no free MoS_2 can be observed (as shown in Figure 4a,c,e), indicating the relatively strong interfacial interaction between MoS_2 and RGO.

Figure S7 (Supporting Information) depicts the cyclic voltammetry (CV) curves of MG-3 in the voltage range of 0.01–3.0 V. The cathodic peaks at 0.89 and 0.71 V are ascribed to the two-step insertion of Na^+ into MoS_2.[3a,17] The broad peak located at 0.35 V could be associated with electrolyte decomposition to form solid electrolyte interphase (SEI) layer and the reversible conversion reaction: $MoS_2 + 4Na^+ + 4e^- \leftrightarrow Mo + 2Na_2S$.[12b] According to previous investigations, the SEI is composed of inorganic and organic layers around the particles.[18] The organic layers can form and dissolve reversibly, which contributes to the reversible capacity. On the contrary, the formation of an inorganic layer is an irreversible process. In addition, a sharp peak at about 0.01 V is found, which can

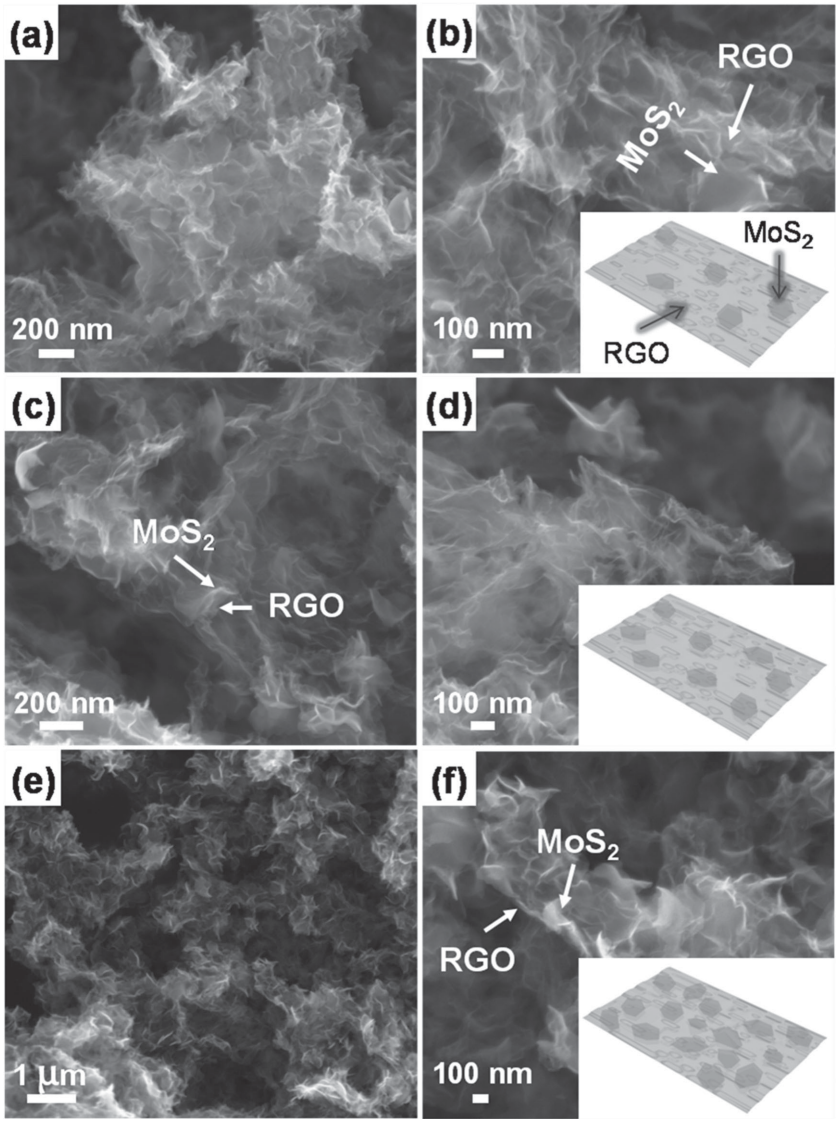

Figure 3. SEM images of a,b) MG-1, c,d) MG-2, and e,f) MG-3, showing the microstructural features of the nanocomposites, the insets show the corresponding schematic illustrations of the composites.

be assigned to the Na-ion insertion into RGO interlayers.[19] From the second cycle, the CV curves overlap perfectly, indicating the high reversibility of the MG-3 electrode. Based on the reversible capacity of bare MoS_2 (590 mA h g^{-1}) and RGO (195 mA h g^{-1}), in combination with their weight ratios in MG-*x* composites, the nominal capacities of MG-*x* samples can be calculated, which are shown in **Figure 5**d. The galvanostatic charge–discharge curves of MG-1, MG-2, and MG-3 electrodes at a current density of 20 mA g^{-1} are shown in Figure 5a–c. In the first discharge process, all of the MG-*x* samples show two plateaus in the range of 1.1–0.5 V, which are in good agreement with the CV curves, corresponding to the Na^+ intercalation processes in MoS_2 layers. It is noted that the MG-*x* electrodes deliver lower charge capacities than the corresponding discharge capacities, which could be ascribed to the irreversible formation of SEI layer. Interestingly, all MG-*x* samples exhibit reversible capacities exceeding the nominal values (Figure 5d). In particular, MG-3 with maximum heterointerfacial areas achieved a reversible capacity of 702 mA h g^{-1}, which is much higher than the nominal value of the total sum ($590 \times 0.687 + 195 \times 0.313 = 466$ mA h g^{-1}). This clearly indicates a synergistic effect for the enhancement of Na^+ storage capacity, which is beyond the simple principle of superposition between RGO and MoS_2. With increasing interfacial contact between RGO and MoS_2 (e.g., increasing the MoS_2 ratio), the enhanced capacity originating from the synergistic effect increases correspondingly. The increased capacities for MG-1, MG-2, and MG-3 electrodes are 84, 160, and 236 mA h g^{-1}, respectively. This result strongly suggests the correlation between the 2D heterointerface and the sodium-ion storage in MoS_2/RGO composites. This means that the composite with more heterointerfacial areas has higher Na^+ storage capacity. The favorable interfacial interaction also leads to a significantly improved cycling performance of the MG-3 compared with the bare MoS_2. As shown in Figure 5e, bare MoS_2 electrode suffers seriously from quick capacity decay. After 100 cycles, the MoS_2 electrode only delivers a capacity of 93 mA h g^{-1}. This could be due to significant volume change and mechanical stress during sodium ion insertion/extraction processes, which induces failure of the electrode, loss of contact between active materials and the current collector, and poor cycling stability. For MG-*x* electrodes, MG-1 with the highest RGO ratio exhibited the best cycling stability, which maintained 61.3% of the capacity obtained in the second cycle after 100 cycles at a current density of 20 mA g^{-1}. While the capacity retentions of MG-2 nanocomposites with the moderate RGO ratio and MG-3 nanocomposites with the lowest RGO ratio are 61.2% and 49.0%, respectively. This could be ascribed to that RGO can effectively buffer the volume change of MoS_2 during repeated sodiation/desodiation processes.[5b]

To gain an in-depth understanding of the role of the MoS_2/RGO heterointerfaces on the performance of electrochemical Na^+ storage, density functional theory (DFT) calculations using the Dmol^3 package[20] have been performed to calculate the adsorption and diffusion behaviors of Na on MoS_2 and MoS_2/RGO heterointerface. We first investigated MoS_2/RGO system, in which RGO exists as perfect pristine graphene (MoS_2/graphene). The adsorption behavior of Na on both monolayer MoS_2 and MoS_2/graphene heterostructures are considered, with the results summarized in **Table 1**. There are three possible positions for Na adsorption on monolayer MoS_2, as numbered in **Figure 6**a. However, the structure with the Na atom adsorbed at the hallow site of a MoS_2 ring (Figure 6b) has the lowest

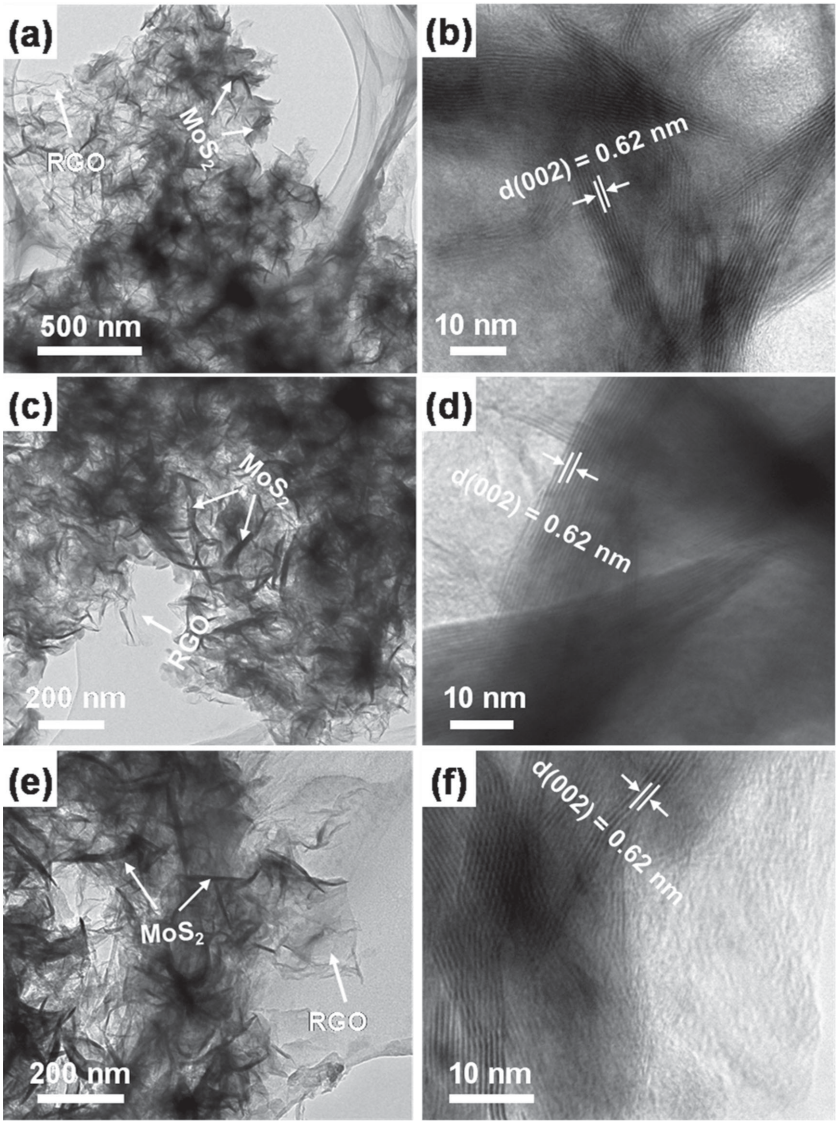

Figure 4. TEM images of MG-*x* composites. a,b) MG-1, c,d) MG-2, and e,f) MG-3.

energy, and it is set to be 0. The adsorption energy of the Na in Figure 6b is –1.49 eV, which is modest for Na storage and diffusion. Based on Mulliken atomic charge analysis, it is found that the Na atom transfers 0.709 *e* to MoS_2, which is promising because more than 2/3 of the valence electrons can be transferred. The diffusion path of the Na atom on MoS_2 from the energy minimum adsorption site 1 to the second energy minimum adsorption site 2 is calculated through linear synchronous transition/quadratic synchronous transit (LST/QST) and nudged elastic band (NEB) methods. The result is shown in Figure 6e. The atomic structure of the initial state (IS), transition state (TS), and final state (FS) is also provided in this figure. At TS, the Na atom moves from the hollow site of the hexagon toward the top site of a Mo atom, and locates at the bridge site of two S atoms. The diffusion barrier is only ≈86 meV, indicating the excellent mobility of Na atom on MoS_2.

For both MC and SC structured MoS_2/graphene heterointerfaces, there are six representative positions for Na adsorption (Figure S8, Supporting Information). The energy of a Na atom adsorbed at the top of a Mo atom (Figure S8b, Supporting Information) is the lowest and set to be 0. Previous investigations show that Li atoms prefer to accommodate themselves between MoS_2 and graphene layers.[21] However, it is found that both MC and SC structures with the Na atom adsorbed on the MoS_2 surface have the lowest energies, which indicates that the Na atom prefers to be adsorbed on the MoS_2 in the MoS_2/graphene heterointerface. Moreover, the presence of graphene changes the adsorption behavior of the Na atom on MoS_2. As discussed, the Na atom adsorbed at the hallow site of a MoS_2 hexagon ring on the pristine MoS_2 monolayer has the lowest energy. On the contrary, our calculation results show that the energy differences for the three different adsorption sites on the MoS_2/graphene heterostructure are very small (<0.5 meV C^{-1}), which suggests that all the three representative adsorption sites on the surface of MoS_2 in the MoS_2/graphene heterointerface are possible.

The interfacial interaction between MoS_2 and graphene can enhance the adsorption of the Na atom while maintaining the efficient diffusion of Na. As shown in Table 1, the adsorption energy (E_{ad}) of the Na atom is –2.59 and –2.57 eV for MC and SC structures, respectively, which are much higher than the adsorption energy –1.49 eV of a Na atom on a monolayer MoS_2. In addition, ≈0.7 *e* of the Na atom adsorbed into the MoS_2 surface in both MC and SC structures is transferred to the MoS_2 layer, which is very similar to the amount 0.709 *e* transferred in the case of monolayer MoS_2. The diffusion of Na on MoS_2 in the MoS_2/graphene heterostructure is also investigated. Because the structures of the Na atom adsorbed at three sites on the MoS_2 layer have very closed energies, the diffusions among the three structures in both MC and SC structures should all be considered, as shown in Figure 6f,g. After LST/QST and NEB calculations, it is found that the diffusion barriers among the three adsorption configurations are similar to each other for both MC and SC structures. However, the diffusion from the hallow position of a MoS_2 ring to the top site of a S atom in a MC structure has the lowest diffusion barrier of 0.082 eV, while it is 0.085 eV for the diffusion from the hallow position of a MoS_2 ring to the top site of a S atom in a SC structure, which are also almost the same as that in a monolayer MoS_2 (0.086 eV). Therefore, the diffusion can occur effectively at room temperature when the barrier is lower than 0.75 eV. Consequently, the diffusion of Na atoms on the MoS_2 surface is fast on both the MoS_2 surface and the MoS_2/graphene heterointerface. Based on above results, it is concluded that the presence of a graphene layer does not change the amount of electrons transferred from Na atoms to MoS_2 or

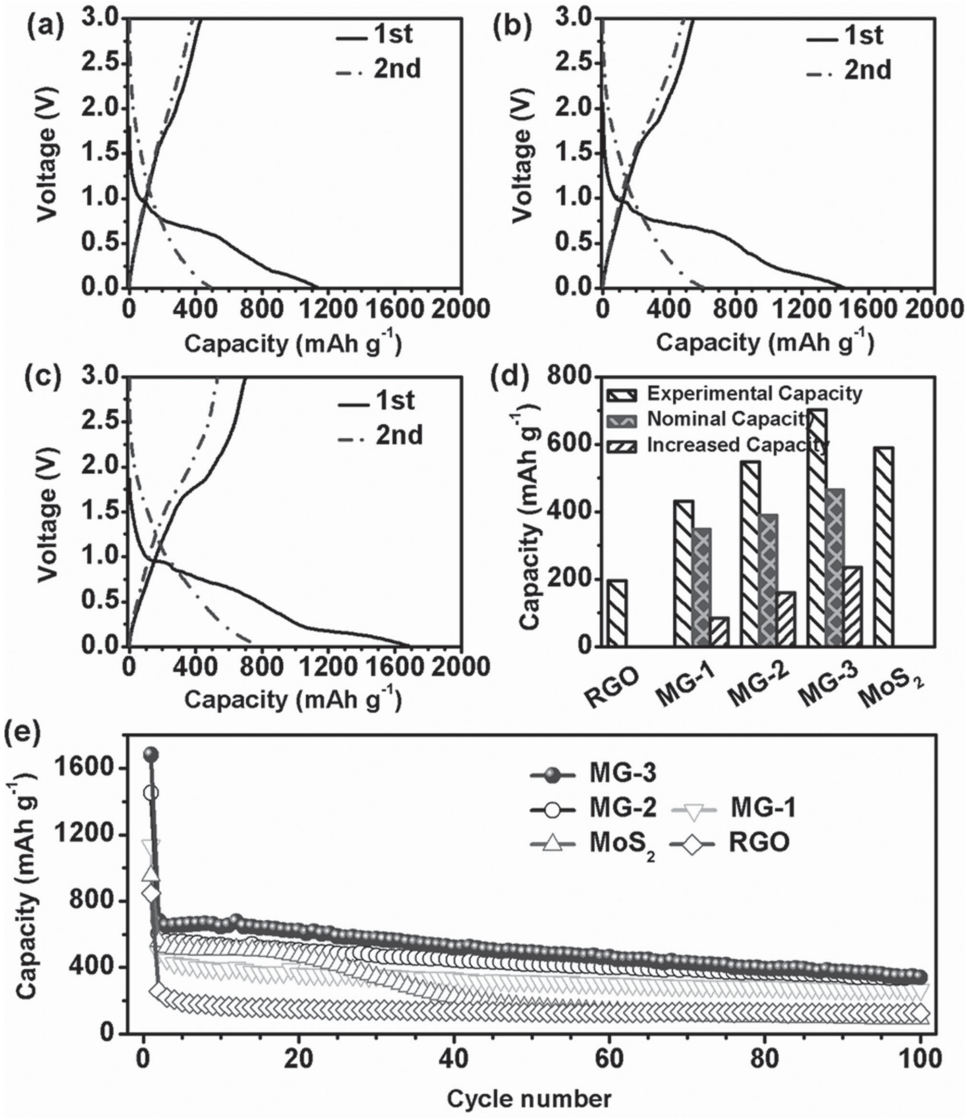

Figure 5. Galvanostatic charge–discharge profiles of a) MG-1, b) MG-2, and c) MG-3. d) Initial reversible capacities of RGO, MG-*x*, and MoS_2 at a current density of 20 mA g^{-1}, and the nominal capacities based on experimental values. The blue bars indicate the increased capacities due to the intimate MoS_2/RGO heterointerface. e) Cycling performance of MG-3, MoS_2, and RGO at a current density of 20 mA g^{-1}.

the diffusion barrier, but increases the adsorption energy of Na atoms on the MoS_2 surface, which indicates more Na atoms can be trapped in the MoS_2/graphene heterointerface.

The band structures of MoS_2 before and after Na atom adsorption are shown in **Figure 7**a,b. Pristine monolayer MoS_2 has ≈1.8 eV direct band gap at *K*-point, which is consistent with the reported values of 1.62 eV[22] and 1.8 eV.[23] After Na atom adsorption, the Fermi level shifts up ≈1.5 eV compared with bare MoS_2, indicating the strong *n*-type doping of MoS_2, which is contributed by large amount of electron transfer from the Na atom to the MoS_2 layer. However, the Na-MoS_2 system still has a wide band gap of 1.74 eV, which hinders the transport of electrons during charge–discharge. MoS_2/graphene heterointerface can improve electronic conductivity compared with bare MoS_2. The band structure of the bilayer MoS_2/graphene system in both MC and SC structures, with and without Na atom adsorption, is calculated and shown in Figure 7c–f. To clearly show the effect of graphene on the conductivity of the MoS_2/graphene heterointerface, the band structure of pristine graphene is also provided in Figure 7c,e, from which it is clearly shown that the bilayer system has a near zero band gap and similar conductive behavior as pristine graphene at the Dirac *K*-point. On the other hand, the presence of the MoS_2 layer also changes the band structure of graphene, where the bands in the valence band away from the Dirac *K*-point shift further away from the Dirac *K*-point in both MC and SC structures. However, the distances of such bands from the Dirac *K*-point in MC and SC structures are different owing to the different stacking configurations. After Na adsorption at its preferred position, the Fermi level shifts upward and *n*-type doping is present, which is similar to the case of monolayer MoS_2. In MC and SC, the Fermi level shifts ≈0.36 and ≈0.30 eV in MC

Table 1. The total energy of MoS_2 and the MoS_2/graphene heterostructure with a Na atom adsorbed at representative positions, the corresponding adsorption energy of the Na atom and the charge transferred from Na atom to MoS_2 or MoS_2/graphene bilayer system are also provided.

	Na Position	Total energy [meV C^{-1}]	E_{ad} [eV]	Q [e]
MoS_2 monolayer	1	0	−1.49	0.709
	2	14.8	−0.75	0.703
	3[a)]	0	−1.49	0.709
MoS_2/graphene	a	0.54	−2.56	0.706
MC	b	0	−2.59	0.700
	c	0.016	−2.59	0.699
	d	8.29	−2.18	0.866
	e	6.66	−2.26	0.896
	f	3.54	−2.41	0.676
MoS_2/graphene	a	12.72	−2.54	0.698
SC	b	12.17	−2.57	0.692
	c	12.20	−2.57	0.692
	d	24.77	−1.94	0.809
	e	21.91	−2.08	0.831
	f	17.55	−2.30	0.698

[a)]The Na atom would diffuse to position 1 automatically. 1–3 denote the possible adsorption position of Na atom as shown in Figure 6a. a–f denote the corresponding adsorption positions as shown in Figure S8a–f (Supporting Information).

and SC structures, respectively, while it shifts ≈1.5 eV in monolayer MoS_2. This difference is induced by the presence of the graphene layer, which receives part of the transferred electrons of Na atoms from the MoS_2 layer. The computational calculations clarify the unique role of the MoS_2/graphene heterointerface for enhancing the Na storage performance, including the increase of the conductivity of the MoS_2/graphene bilayer system, the capture of more Na, and the maintenance of high diffusion mobility of Na atoms on the MoS_2 surface, and high electron transfer efficiency from Na to MoS_2. Due to the presence of the MoS_2/graphene heterointerface, more Na atoms can be adsorbed with large amounts of electrons transferred to the MoS_2 layer and high diffusion mobility on the MoS_2 surface, while the graphene is the highly conductive conductor to transport the transferred electrons. This would result in high Na storage capacity and excellent rate capability.

Since there are residual oxygen-containing moieties (such as hydroxyl and epoxy groups) in RGO, we also consider the effect of such residual oxygen-containing groups on Na adsorption and diffusion in the MoS_2/RGO heterointerface. Due to similar energy and properties for both MC and SC configurations, the MC configuration is taken as the example to investigate the effects of hydroxyl and epoxy groups in RGO. After considering all possible positions of hydroxyl and epoxy groups, it is found that the epoxy or hydroxyl group prefers to locate below the graphene layer as shown in Figure S9a,b (Supporting Information). The interaction between RGO and MoS_2 is the weak van der Waals interaction with the interaction energy of

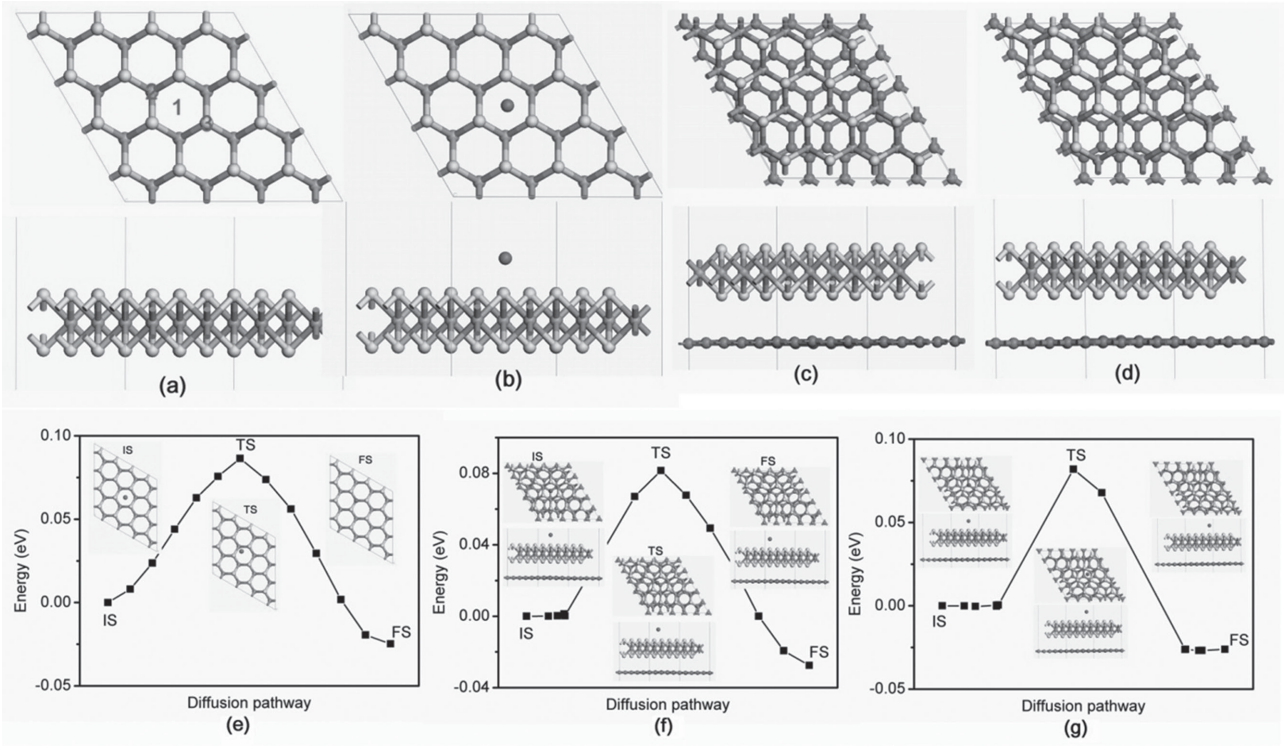

Figure 6. a) Atomic structure of monolayer MoS_2 supercell in the simulation, the numbers denote the possible adsorption position of Na atom. b) The favorite structure of monolayer MoS_2 with a Na atom adsorbed. Configuration of c) MC bilayer and d) SC bilayer. The energy minimum diffusion pathway of a Na atom e) on the monolayer MoS_2, f) in MC bilayer, and g) in SC bilayer. The insets in (e–g) show the atomic structure of initial state (IS), transition state (TS), and final state (FS).

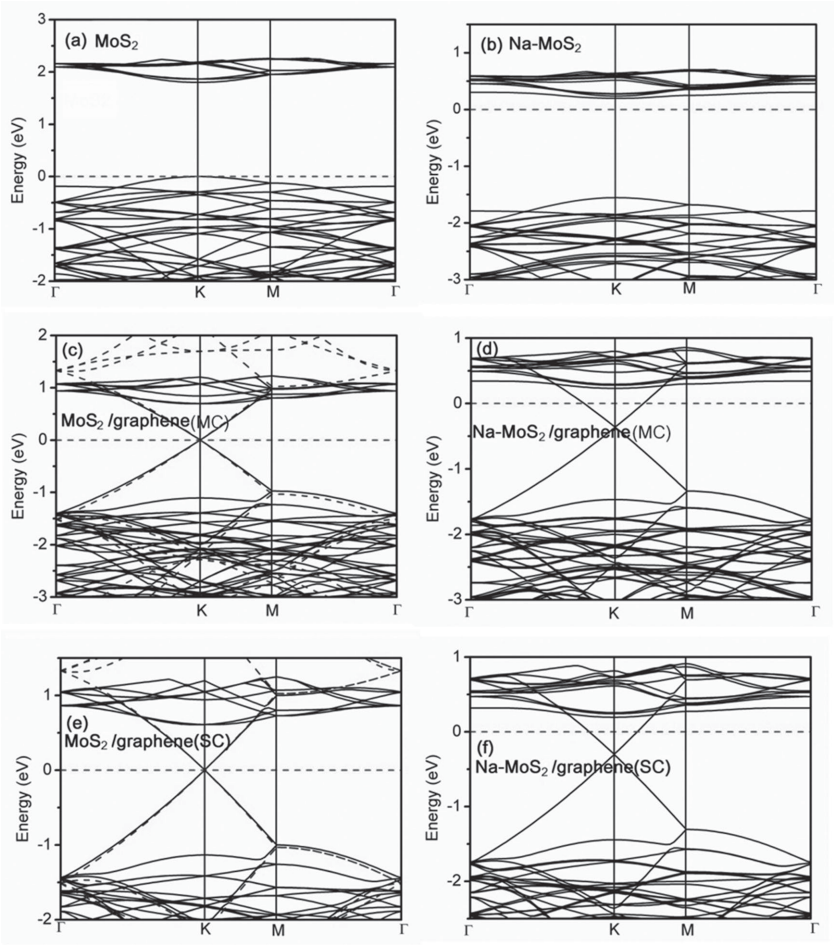

Figure 7. The band structures of a) monolayer MoS_2, c) MoS_2/graphene bilayer with MC structure, and e) MoS_2/graphene bilayer with SC structure. b,d,f) The corresponding band structure after the adsorption of Na. The dashed curves are the band structure of pristine graphene and dashed line denotes the Fermi level.

≈0.03 eV C^{-1}, which is slightly higher than that in MoS_2/RGO system without oxygen-containing groups (MoS_2/graphene). For the adsorption of Na ions, similar to that demonstrated in Figure S8 (Supporting Information), it is found that the Na atom prefers to adsorb on top of Mo atom. The adsorption energies are −2.64 and −2.75 eV in MoS_2/RGO system with epoxy and hydroxyl group, respectively. This is slightly stronger than that in MoS_2/RGO system without oxygen function groups. With the presence of the oxygen-containing groups, Na atom transfers ≈0.71 *e* to MoS_2, which is higher than that in MoS_2/RGO system without oxygen-containing. The corresponding diffusion behavior was also investigated and the energy minimum diffusion pathway is shown in Figure S9c,d (Supporting Information). The diffusion barriers are 0.107 and 0.16 eV in MoS_2/RGO system with epoxy and hydroxyl groups, respectively. This indicates that the high mobility of Na atom in MoS_2/RGO heterostructure can be maintained in the presence of epoxy and hydroxyl groups in RGO. Consequently, even with residual oxygen-containing moieties in RGO, the MoS_2/RGO heterostucture is still superior for Na storage over the bare MoS_2, which maintains high diffusion mobility of Na atoms on MoS_2 surface and high electron transfer efficiency from Na to MoS_2.

To understand the conductivity changes in the presence of oxygen-containing groups, the band structures of the MoS_2/RGO with epoxy and hydroxyl groups are shown in Figure S10 (Supporting Information). The band gap of MoS_2 decreases from ≈1.8 to ≈0.5 eV after combining with RGO containing epoxy group, and no band gap is found in MoS_2/RGO with hydroxyl group. After Na adsorption, the Fermi level shifts up ≈0.5 and ≈0.25 eV in MoS_2/RGO system with epoxy and hydroxyl groups, respectively. The corresponding band gap of MoS_2/RGO with epoxy group disappears, while it is ≈0.05 eV for MoS_2/RGO with hydroxyl group. Therefore, the conductivity of MoS_2 is improved after coupling with RGO containing oxygen functional groups, i.e., the oxygen-containing groups in RGO does not change electrochemical properties for sodium-ion batteries.

The in situ hybridization of MoS_2 and RGO plays an important role in constructing MoS_2/RGO heterostructures with enhanced electrochemical performances for Na^+ storage. First, RGO as macromolecular surfactants can effectively stabilize MoS_2 nanosheets with high surface energy, realizing high-dispersive MoS_2 supported on RGO. As a result, more reactive sites are available for the electrode/electrolyte interaction. Second, this soft integration method enables high-quality electrical contact between MoS_2 and RGO, which ensures the functionality of the MoS_2/RGO heterointerface for Na-ion storage performance. The enhanced electrical conductivity of MG-3 due to the intimate interfacial interaction is confirmed by electrochemical impedance spectroscopy (EIS) measurements. **Figure 8**a shows the Nyquist plots of EIS for MG-3 and MoS_2. The Nyquist plots consist of a single depressed semicircle in the high-medium frequency region and an inclined line at low frequency. Obviously, MG-3 features a much smaller semicircle diameter than that of MoS_2, indicating a high electrical conductivity and a rapid charge-transfer reaction for Na^+ insertion and extraction. The fast charge-transfer ability leads to an excellent high-rate performance of the MG-3 electrode. Continuous cycling was carried out at the following current densities: 20, 40, 80, 160, 320, and 640 mA g^{-1}. As shown in Figure 8b, the MG-3 electrode demonstrates a good high rate capability. Even when the current density increases to 640 mA g^{-1}, the MG-3 electrode retains a capacity of 352 mA h g^{-1}, which is 50.2% of the capacity obtained at 20 mA g^{-1}. Furthermore, when the current density is reversed to 40 mA g^{-1}, the MG-3 electrode can recover its capacity after 45 cycles, suggesting its excellent rate performance and cycling stability. However, the bare MoS_2 electrode suffers from continuous capacity fading and it fails to recover the capacity when the current density reversed to the low value.

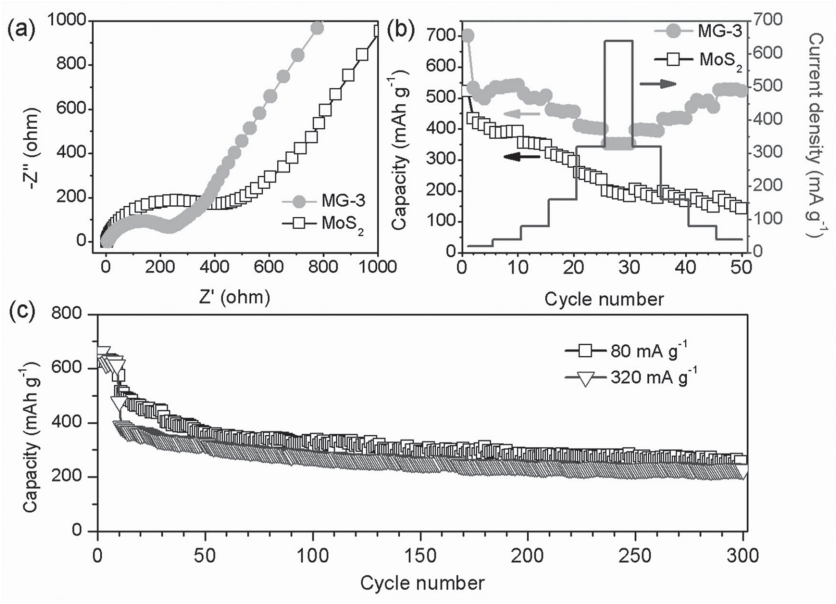

Figure 8. a) Nyquist plots of MG-3 and MoS_2 as anode materials in the charged state (3.0 V vs Na^+/Na). b) Rate performance of MG-3 and MoS_2 electrodes. c) Discharge capacity as a function of cycle number of MG-3 electrode from the second cycle at high current densities of 80 and 320 mA g^{-1}. The first 20 cycles were tested at a current density of 20 mA g^{-1}.

From Figure 8c it can be seen that the MG-3 electrode also exhibits good cycling performance at high current densities. After 300 cycles, MG-3 retained Na^+ storage capacities of 254 and 227 mA h g^{-1} at 80 and 320 mA g^{-1}, respectively.

The promising electrochemical performance of MoS_2/RGO nanocomposites could be attributed to the 2D heterointerfaces between MoS_2 and RGO, which results in a synergistic effect toward the Na^+ storage over MoS_2/RGO. In particular, the van der Waals interaction between RGO and MoS_2 leads to an intimate interfacial interaction, which helps ameliorate the restacking and aggregation of MoS_2 nanosheets. Consequently, more active sites are available for the electrode/electrolyte interaction. The intimate interfacial interaction also improves the interfacial electron transfer during sodiation/desodiation, which can maximize the conductivity of RGO. Moreover, without deteriorating the diffusion behaviors of Na and the electron transfer efficiency from Na to MoS_2, MoS_2/RGO heterointerfaces show the ability to enhance the adsorption of Na, which is also beneficial for the Na-ion storage in sodium-ion batteries.

3. Conclusion

In summary, a series of sheet-on-sheet structured MoS_2/RGO nanocomposites with different heterointerfacial areas have been successfully prepared by a facile bottom-up hydrothermal method followed by a calcination process. The synergistic effect contributes to the improved capacity for Na-ion storage through increasing the heterointerfacial area. In particular, MG-3 with maximum heterointerfacial areas can deliver a reversible capacity of 702 mA h g^{-1} for sodium-ion batteries. The MG-3 electrode also demonstrated excellent rate capabilities. Even at a high current density of 640 mA g^{-1}, MG-3 can still deliver a capacity of 352 mA h g^{-1}. It is found that the 2D MoS_2/RGO heterointerface can increase the conductivity of MoS_2 and capture more Na atoms, while maintaining the high diffusion mobility of Na on the MoS_2 surface and high electron transfer efficiency from Na to MoS_2. Our findings could enhance the understanding of 2D graphene-based heterostructures, which is important for the rational design of high-performance electrode materials for sodium-ion batteries.

4. Experimental Section

Sample Preparation: Graphene oxide (GO) nanosheets were synthesized from natural graphite powders by a modified Hummers' method.[24] The MoS_2/RGO nanocomposite was then produced by a hydrothermal method. In a typical synthesis process, PMA was mixed with 20 mL GO aqueous suspension (1 mg mL^{-1}) by ultrasonication using a Brandson Digital Sonifer (S450D, 40% amplitude). After ultrasonication for 0.5 h, L-cysteine was added and mechanically stirred for another 0.5 h. For the preparation of MG-1, MG-2, and MG-3, the concentration of PMA was 0.81, 1.15, and 1.62 mg mL^{-1}, respectively, where the concentration of L-cysteine was fixed to be 50 mg mL^{-1}. Then, the mixed precursor solution was heated to 200 °C in a Teflon-lined autoclave (25 mL in capacity) and maintained at 200 °C for 24 h. The precipitates were collected, and washed with distilled water and ethanol several times. The products were collected after drying at 60 °C in a vacuum oven overnight, which was then annealed at 800 °C for 2 h in argon atmosphere.

Structural and Physical Characterization: The crystal structure and phases of the as-prepared materials were characterized by X-ray diffraction (XRD, Siemens D5000) using Cu Kα radiation with a scanning step of 0.02° s^{-1}. The morphology was analyzed by field emission scanning electron microscopy (FESEM, Zeiss Supra 55VP). The details of the morphology were further characterized by transmission electron microscopy (TEM) and high-resolution TEM (HRTEM, JEOL JEM-2011). The elemental analysis was conducted on Zeiss EVO MA 15 SEM equipped with an energy-dispersive X-ray spectrometer (EDX). The MoS_2 loading mass was measured using a TGA/differential thermal analysis (DTA) analyzer (TA Instruments, SDT 2960 module, New Castle, DE, USA) at a heating rate of 10 °C min^{-1} in air from room temperature to 600 °C. Raman spectra were collected with a Renishaw inVia Raman spectrometer system (Gloucestershire, UK) equipped with a Leica DMLB microscope (Wetzlar, Germany) and a Renishaw He-Ne laser source producing 17 mW at 633 nm.

Cell Assembly and Electrochemical Testing: The electrodes were prepared by dispersing the as-prepared material (70 wt%), carbon black (20 wt%), and poly (vinylidene fluoride) binder (PVDF, 10 wt%) in *N*-methyl-2-pyrrolidone (NMP) to form a slurry. The resultant slurry was pasted onto copper foil using a doctor blade and dried in a vacuum oven for 12 h, followed by pressing at 200 kg cm^{-2}. The mass of each electrode was around 1.0 mg cm^{-2}. Electrochemical measurements were carried out using two-electrode coin cells with Na metal as counter and reference electrode and glass microfiber (Whatman) as the separator. The CR2032-type coin cells were assembled in an argon-filled glove box (UniLab, Mbraun, Germany). The electrolyte solution was 1 M $NaClO_4$ dissolved in a mixture of ethylene carbonate (EC) and propylene

carbonate (PC) with a volume ratio of 1:1. The charge–discharge measurements were performed at different current densities in the voltage range from 0.01 to 3 V versus Na^+/Na using a computer-controlled Neware Battery Testing system. For the MG-*x* electrode, the obtained specific capacities are based on the total mass of MG-*x*. Cyclic voltammetry (CV) was conducted by using a CHI 660C electrochemical workstation between 0.01 and 3 V versus Na^+/Na with a scan rate of 0.1 mV s^{-1}. For the electrochemical impedance spectroscopy (EIS), the excitation amplitude applied to the cells was 5 mV.

DFT Calculations: The spin-unrestricted DFT calculations were carried out by using a Dmol^3 package.[20] Exchange-correlation functions are taken as generalized gradient approximation (GGA) with Perdew–Burke–Ernzerhof (PBE).[25] DFT semicorepseudopotentials (DSPPs) core treatment was implemented for relativistic effects, which replaced core electrons by a single effective potential. Double numerical plus polarization (DNP) was employed as the basis set. The convergence tolerance of energy of 10^{-5} hartree was taken (1 hartree = 27.21 eV), and the maximal allowed force and displacement were 0.002 hartree $Å^{-1}$ and 0.005 Å, respectively. In the simulation, three–dimensional periodic boundary conditions were taken. The simulation cell consisted of a 4×4 MoS_2 supercell. The *k*-point was set to $5 \times 5 \times 1$, and all atoms were allowed to relax according to previous reports. After structure relaxations, the density of states (DOS) and band structure were calculated with a finer *k*-point grid of $15 \times 15 \times 1$. The DFT+D method within the Grimme scheme was used in all calculations to consider the van der Waals forces,[26] and 18 Å vacuum over the MoS_2 layer or MoS_2/RGO was taken to minimize the interlayer interactions. For the diffusion of Na atoms on monolayer MoS_2, double layer MoS_2 and MoS_2/RGO, LST/QST, and NEB tools in the DMOL^3 code were employed. The adsorption energy (E_{ad}) of the Na atom on MoS_2 can be defined as follows:

$$E_{ad} = E_{MoS2+Na} - (E_{MoS2} + E_{Na}) \quad (1)$$

where $E_{MoS2+Na}$, E_{MoS2}, and E_{Na} are the total energies of monolayer MoS_2 with one Na atom adsorbed, monolayer MoS_2 and one Na atom in the same slab, respectively. The interaction energy E_{int} between MoS_2 and RGO layers can be determined by the equation:

$$E_{int} = E_{MoS2+RGO} - (E_{MoS2} + E_{RGO}) \quad (2)$$

where $E_{MoS2+RGO}$, E_{MoS2}, and E_{RGO} are the total energies of MoS_2/RGO bilayer structure, monolayer MoS_2 and monolayer RGO in the same slab, respectively. The adsorption energy E_{ad} of the Na atom on MoS_2/RGO bilayer structure can be calculated by the equation:

$$E_{ad} = E_{MoS2/RGO+Na} - \left(E_{MoS2/RGO} + E_{Na}\right) \quad (3)$$

where $E_{MoS2/RGO+Na}$ is the total energies of the MoS_2/RGO structure with one Na atom adsorbed.

Supporting Information

Supporting Information is available from the Wiley Online Library or from the author.

Acknowledgements

X.X. and Z.A. contributed equally to this work. This original research was proudly supported by the Commonwealth of Australia through the Automotive Australia 2020 Cooperative Research Centre (AutoCRC) and the Fundamental Research Funds for the Central Universities of China (NE2014301). Z.A. would also like to acknowledge the financial support from the Chancellor's Postdoctoral Research Fellowship Program of the University of Technology, Sydney. This research was also supported by the National Computational Infrastructure (NCI) through the merit allocation scheme and used NCI resources and facilities in Canberra, Australia.

Received: November 18, 2014
Revised: December 26, 2014
Published online: January 22, 2015

[1] a) V. Palomares, P. Serras, I. Villaluenga, K. B. Hueso, J. Carretero-Gonzalez, T. Rojo, *Energy Environ. Sci.* **2012**, *5*, 5884; b) M. D. Slater, D. Kim, E. Lee, C. S. Johnson, *Adv. Funct. Mater.* **2013**, *23*, 947; c) Z. Jian, C. Yuan, W. Han, X. Lu, L. Gu, X. Xi, Y.-S. Hu, H. Li, W. Chen, D. Chen, Y. Ikuhara, L. Chen, *Adv. Funct. Mater.* **2014**, *24*, 4265; d) C. Li, C. Yin, L. Gu, R. E. Dinnebier, X. Mu, P. A. van Aken, J. Maier, *J. Am. Chem. Soc.* **2013**, *135*, 11425.

[2] a) J. Sangster, *J. Phase Equilib. Diffus.* **2007**, *28*, 571; b) S. Komaba, W. Murata, T. Ishikawa, N. Yabuuchi, T. Ozeki, T. Nakayama, A. Ogata, K. Gotoh, K. Fujiwara, *Adv. Funct. Mater.* **2011**, *21*, 3859.

[3] a) J. Park, J.-S. Kim, J.-W. Park, T.-H. Nam, K.-W. Kim, J.-H. Ahn, G. Wang, H.-J. Ahn, *Electrochim. Acta* **2013**, *92*, 427; b) Z. Hu, L. Wang, K. Zhang, J. Wang, F. Cheng, Z. Tao, J. Chen, *Angew. Chem.* **2014**, *126*, 13008; c) C. Zhu, X. Mu, P. A. van Aken, Y. Yu, J. Maier, *Angew. Chem. Int. Ed.* **2014**, *53*, 2152.

[4] D. Su, S. Dou, G. Wang, *Chem. Commun.* **2014**, *50*, 4192.

[5] a) P. K. Dutta, U. K. Sen, S. Mitra, *RSC Adv.* **2014**, *4*, 43155; b) T. Zhou, W. K. Pang, C. Zhang, J. Yang, Z. Chen, H. K. Liu, Z. Guo, *ACS Nano* **2014**, *8*, 8323.

[6] a) X. Xie, D. Su, S. Chen, J. Zhang, S. Dou, G. Wang, *Chem. Asian J.* **2014**, *9*, 1611; b) B. Qu, C. Ma, G. Ji, C. Xu, J. Xu, Y. S. Meng, T. Wang, J. Y. Lee, *Adv. Mater.* **2014**, *26*, 3854.

[7] a) C. N. R. Rao, A. K. Sood, K. S. Subrahmanyam, A. Govindaraj, *Angew. Chem. Int. Ed.* **2009**, *48*, 7752; b) P.-P. Wang, H. Sun, Y. Ji, W. Li, X. Wang, *Adv. Mater.* **2014**, *26*, 964.

[8] a) L. Britnell, R. Gorbachev, R. Jalil, B. Belle, F. Schedin, A. Mishchenko, T. Georgiou, M. Katsnelson, L. Eaves, S. Morozov, *Science* **2012**, *335*, 947; b) L. Britnell, R. Ribeiro, A. Eckmann, R. Jalil, B. Belle, A. Mishchenko, Y.-J. Kim, R. Gorbachev, T. Georgiou, S. Morozov, *Science* **2013**, *340*, 1311; c) B. Hunt, J. D. Sanchez-Yamagishi, A. F. Young, M. Yankowitz, B. J. LeRoy, K. Watanabe, T. Taniguchi, P. Moon, M. Koshino, P. Jarillo-Herrero, R. C. Ashoori, *Science* **2013**, *340*, 1427; d) K. Roy, M. Padmanabhan, S. Goswami, T. P. Sai, G. Ramalingam, S. Raghavan, A. Ghosh, *Nat. Nanotechnol.* **2013**, *8*, 826; e) M. Sup Choi, G.-H. Lee, Y.-J. Yu, D.-Y. Lee, S. Hwan Lee, P. Kim, J. Hone, W. Jong Yoo, *Nat. Commun.* **2013**, *4*, 1624; f) L. Wang, I. Meric, P. Y. Huang, Q. Gao, Y. Gao, H. Tran, T. Taniguchi, K. Watanabe, L. M. Campos, D. A. Muller, J. Guo, P. Kim, J. Hone, K. L. Shepard, C. R. Dean, *Science* **2013**, *342*, 614; g) Z.-G. Chen, Z. Shi, W. Yang, X. Lu, Y. Lai, H. Yan, F. Wang, G. Zhang, Z. Li, *Nat. Commun.* **2014**, *5*, 4461; h) H. Fang, C. Battaglia, C. Carraro, S. Nemsak, B. Ozdol, J. S. Kang, H. A. Bechtel, S. B. Desai, F. Kronast, A. A. Unal, G. Conti, C. Conlon, G. K. Palsson, M. C. Martin, A. M. Minor, C. S. Fadley, E. Yablonovitch, R. Maboudian, A. Javey, *Proc. Natl. Acad. Sci. U.S.A.* **2014**, *111*, 6198; i) J. Y. Kwak, J. Hwang, B. Calderon, H. Alsalman, N. Munoz, B. Schutter, M. G. Spencer, *Nano Lett.* **2014**, *14*, 4511.

[9] K. Chang, W. Chen, *ACS Nano* **2011**, *5*, 4720.

[10] R. Chen, T. Zhao, W. Wu, F. Wu, L. Li, J. Qian, R. Xu, H. Wu, H. M. Albishri, A. S. Al-Bogami, D. A. El-Hady, J. Lu, K. Amine, *Nano Lett.* **2014**, *14*, 5899.

[11] a) A. Geim, I. Grigorieva, *Nature* **2013**, *499*, 419; b) K. Zhang, F. L. Yap, K. Li, C. T. Ng, L. J. Li, K. P. Loh, *Adv. Funct. Mater.* **2014**,

24, 731; c) J. Lu, L. C. Gomes, R. W. Nunes, A. H. Castro Neto, K. P. Loh, *Nano Lett.* **2014**, *14*, 5133.
[12] a) L. David, R. Bhandavat, G. Singh, *ACS Nano* **2014**, *8*, 1759; b) Y.-X. Wang, S.-L. Chou, D. Wexler, H.-K. Liu, S.-X. Dou, *Chem. Eur. J.* **2014**, *20*, 9607.
[13] Y. Li, H. Wang, L. Xie, Y. Liang, G. Hong, H. Dai, *J. Am. Chem. Soc.* **2011**, *133*, 7296.
[14] K. Chang, W.-X. Chen, H. Li, H. Li, *Electrochim. Acta* **2011**, *56*, 2856.
[15] C. N. R. Rao, A. Nag, *Eur. J. Inorg. Chem.* **2010**, *2010*, 4244.
[16] K. Chang, W. Chen, *Chem. Commun.* **2011**, *47*, 4252.
[17] X. Wang, X. Shen, Z. Wang, R. Yu, L. Chen, *ACS Nano* **2014**, *8*, 11394.
[18] a) P. Poizot, S. Laruelle, S. Grugeon, J.-M. Tarascon, *J. Electrochem. Soc.* **2002**, *149*, A1212; b) K. Edström, T. Gustafsson, J. O. Thomas, *Electrochim. Acta* **2004**, *50*, 397.
[19] a) L. Xiao, Y. Cao, J. Xiao, W. Wang, L. Kovarik, Z. Nie, J. Liu, *Chem. Commun.* **2012**, *48*, 3321; b) L. David, G. Singh, *J. Phys. Chem. C* **2014**, *118*, 28401.
[20] B. Delley, *J. Chem. Phys.* **2000**, *113*, 7756.
[21] R. H. Miwa, W. L. Scopel, *J. Phys.: Condens. Matter* **2013**, *25*, 445301.
[22] Y. Li, D. Wu, Z. Zhou, C. R. Cabrera, Z. Chen, *J. Phys. Chem. Lett.* **2012**, *3*, 2221.
[23] Y. Ma, Y. Dai, M. Guo, C. Niu, B. Huang, *Nanoscale* **2011**, *3*, 3883.
[24] a) W. S. Hummers, R. E. Offeman, *J. Am. Chem. Soc.* **1958**, *80*, 1339; b) M.-Q. Yang, N. Zhang, M. Pagliaro, Y.-J. Xu, *Chem. Soc. Rev.* **2014**, *43*, 8240; c) N. Zhang, Y. Zhang, Y.-J. Xu, *Nanoscale* **2012**, *4*, 5792; d) M.-Q. Yang, Y.-J. Xu, *Phys. Chem. Chem. Phys.* **2013**, *15*, 19102.
[25] J. P. Perdew, K. Burke, M. Ernzerhof, *Phys. Rev. Lett.* **1996**, *77*, 3865.
[26] S. Grimme, *J. Comput. Chem.* **2006**, *27*, 1787.